Disentangling electron-boson interactions on the surface of a familiar ferromagnet

Håkon I. Røst,[1,2] Federico Mazzola,[3,4] Johannes Bakkelund,[1] Anna Cecilie Åsland,[1] Jinbang Hu,[1] Simon P. Cooil,[5] Craig M. Polley,[6] and Justin W. Wells[1,5,*]

[1]*Department of Physics, Norwegian University of Science and Technology (NTNU), NO-7491 Trondheim, Norway*
[2]*Department of Physics and Technology, University of Bergen, 5007 Bergen, Norway*
[3]*Department of Molecular Sciences and Nanosystems, Ca' Foscari University of Venice, 30172 Venice, Italy*
[4]*Istituto Officina dei Materiali, Consiglio Nazionale delle Ricerche, Trieste I-34149, Italy*
[5]*Department of Physics and Centre for Materials Science and Nanotechnology, University of Oslo, 0318 Oslo, Norway*
[6]*MAX IV Laboratory, Lund University, Lund, 22484 Sweden*

(Received 4 November 2022; revised 6 December 2023; accepted 20 December 2023; published 17 January 2024)

We report energy renormalizations from electron-phonon and electron-magnon interactions in spin minority surface resonances on Ni(111). The different interactions are identified, disentangled, and quantified from the characteristic signatures they provide to the complex self-energy and the largely different binding energies at which they occur. The observed electron-magnon interactions exhibit a strong dependence on momentum and the electron energy band position in the bulk Brillouin zone. In contrast, electron-phonon interactions observed from the same bands appear to be relatively momentum and symmetry independent. Additionally, a moderately strong ($\lambda > 0.5$) electron-phonon interaction is distinguished from a near-parabolic spin majority band not crossing the Fermi level.

DOI: 10.1103/PhysRevB.109.035137

I. INTRODUCTION

In condensed matter, the interplay of electrons and other fundamental and collective excitations can induce new and exotic phases of electronic ordering. Perhaps most studied is the coupling between electrons and lattice vibrations (phonons) which can trigger an effective and attractive electron interaction and lead to superconductivity in elementary metals [1]. While low T_C superconductivity can be well explained from electron-phonon coupling (EPC) alone, other and less conventional pairing mechanisms have been suggested as ingredients of high T_C superconductivity [2–5]. In superconducting ferro- and antiferromagnets, electrons can also couple to spin waves (magnons) [6–12]. Electron-magnon interactions are furthermore expected to mediate proximity-induced superconductivity across magnetic interfaces [13–18].

For the experimental study of many-body interactions with electrons, angle-resolved photoemission spectroscopy (ARPES) is the tool of choice as the complete, complex self-energy can be extracted from the measured electronic band structures [19–23]. While EPC has been extensively studied using ARPES, there are only a handful of reports of electron-magnon couplings (EMC) available [24–31]. The majority of these consider couplings only in specific electron bands or over small subregions of reciprocal space. This motivates the need for further investigations of EMC that explore how the interactions can vary between different spin bands and throughout the Brillouin zone (BZ).

Herein we present a thorough study of the many-body interactions present in Ni(111). Electron-phonon and electron-magnon interactions are unraveled from different spin bands, at several different positions in the bulk BZ, and along several high-symmetry directions of the projected bulk BZ (PBZ). The EPC and EMC are disentangled from one another based on their characteristic signatures and contributions to the electron self-energy. The EMC of the spin minority bands exhibits a strong dependence on the electron momentum, i.e., the location within the bulk BZ, both in interaction strength and regarding the participating magnon modes. In contrast, the EPC is much less momentum-dependent and visible with reasonable strength in both the spin minority and majority bands.

First, an overview of the electronic structure of Ni(111) is given in Sec. II A. Next, the different many-body effects observed from its spin majority and minority bands are discussed, disentangled, and quantified in Sec. II B. A summary and final remarks are given in Sec. III. Details about the experiments and the many-body analysis are given in Secs. IV A–IV C and the Supplemental Material [32].

II. RESULTS AND DISCUSSION

A. Electronic structure and surface resonances

An overview of the electronic structure of Ni(111) near the Fermi level (E_F) is shown in Fig. 1. Along the [111] direction the bulk BZ of Ni is projected onto a two-dimensional zone that is hexagonal and threefold symmetric [Fig. 1(a)] [33]. The projected Fermi surface is shown in Fig. 1(b), as measured by ARPES with $h\nu = 21.2$ eV (left) and as calculated from

*Corresponding author: j.w.wells@fys.uio.no

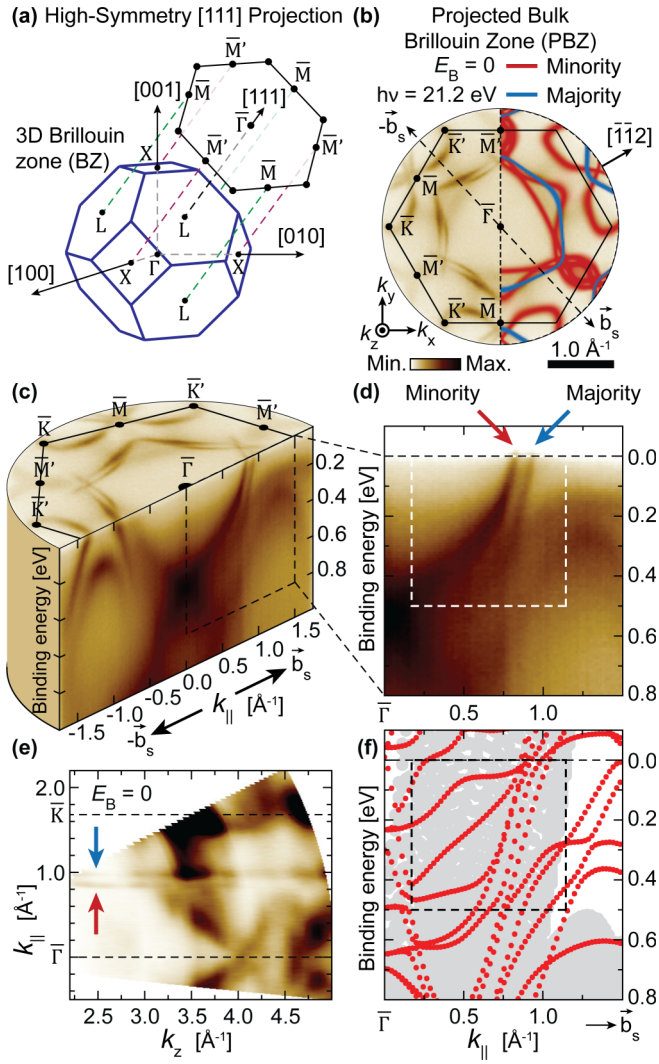

FIG. 1. The electronic structure of Ni(111). (a) Sketch showing the projection of the bulk Brillouin zone of Ni onto the (111) plane. (b) Measured constant energy surface of Ni(111) at E_F (left) and the calculated band structure with free-electron final states (right), both using $h\nu = 21.2$ eV. (c) Volumetric representation of the measured Ni(111) band structure. The energy cut has been performed from $\bar{\Gamma}$ and along the $\pm\mathbf{b}_s$ directions as shown in (b). (d) Measured band structure (E vs $k_{||}$) along the $+\mathbf{b}_s$ direction. A clear spin splitting of the states can be seen close to E_F. The assignment of minority and majority states is based on the density functional theory calculation in (b). (e) Photoemission intensity as a function of final-state wave number k_z. (f) The calculated, unrenormalized spin minority surface states (red) of Ni(111) along the $+\mathbf{b}_s$ direction. The shaded background (gray) represents the surface-projected, spin majority bulk bands. Surface resonance states can be observed near $(E_B, k_{||}) = (0.0\,\text{eV}, 0.82\,\text{Å}^{-1})$.

first principles (DFT) while accounting for the available free-electron final states at this photon energy (right) [20,34,35].

Approximately halfway from $\bar{\Gamma}$ towards the edge of the first PBZ, two different spin minority contours and one spin majority contour can be distinguished near E_F. The mentioned spin bands all meet near the $\bar{M}'$ high-symmetry point, and approximately halfway between $\bar{M}'$ and $\bar{K}$ a maximum separation between the bands is seen. Defining an in-plane momentum vector $\mathbf{b}_s$ ($\propto k_{||}$) from $\bar{\Gamma}$ and towards the PBZ boundary between $\bar{M}'$ and $\bar{K}$ [Fig. 1(b)], the local energy dispersion $E(k_{||})$ of the spin bands can be investigated. An example cut along the directions $\pm\mathbf{b}_s$ is shown in Fig. 1(c) with two prominent spin bands highlighted (dashed rectangle). As further demonstrated in Fig. 1(d), the two bands are nearly parallel and almost straight in the topmost 100 meV near E_F. Based on the free-electron final-state-dependent calculations [Fig. 1(b)], the dispersion furthest away from $\bar{\Gamma}$ at E_F is interpreted as a spin majority band, and the one closer to $\bar{\Gamma}$ as one of two possible spin minority bands.

Notably, a two-dimensional, dispersionless behavior can be observed from the mentioned spin minority and majority bands. While their surrounding energy band features at E_F readily disperse with wave vector $\mathbf{k}_z$ along the bulk $\Gamma \rightarrow$ L direction, the two parallel spin bands appear approximately linear, with little or no $\mathbf{k}_z$ dependence [Fig. 1(e)]. These are common features of states that are localized or quasilocalized perpendicular at the atomic surface where the $\mathbf{k}_z$ symmetry is broken [19].

In Fig. 1(f), the calculated, unrenormalized spin minority surface states of Ni(111) along $\mathbf{b}_s$ are shown, some of which appear to qualitatively resemble the dispersion of the measured spin minority states highlighted in Fig. 1(d). The calculated spin minority states [Fig. 1(f), red] appear to overlap with the projected spin majority states from the bulk (gray), thereby enabling coupling between surface and bulk states through spin-flip scattering processes by the absorption or emission of magnons [24]. A similar overlap is also present between the calculated spin majority surface states and the projected spin minority bulk bands (see the Supplemental Material [32]). Hence the measured, $\mathbf{k}_z$-independent bands in Figs. 1(d) and 1(e) are interpreted as surface resonance states [19,24]. The calculations suggest that a handful of similar states exist near E_F with $k_{||} = 0.7$–0.8 Å^{-1}. Several different resonances should, therefore, in principle, be observable from ARPES measurements.

B. Signatures of electron-boson interactions

The spin bands in Figs. 1(c) and 1(d) contain apparent signs of broadening over the binding energy range $E_B = 0$–400 meV. Typically, such energy broadening can be described by various quasiparticle renormalizations, signaling a reduced lifetime τ and associated increased self-energy Σ for the electron states [21]. One can often assume $\Sigma(\mathbf{k}, \omega)$ to vary slowly with momentum when observed over a narrow range of E vs $\mathbf{k}$, such as within the interaction region of a renormalized electron energy band [36]. The measured ARPES intensity at a temperature T is then proportional to a simplified expression for the spectral function $\mathcal{A}(\mathbf{k}, \omega)$ [20,21]:

$$I(\mathbf{k}, \omega) \propto \mathcal{A}(\mathbf{k}, \omega) = \pi^{-1}\text{Im}\, G(\mathbf{k}, \omega) = \frac{-\pi^{-1}\text{Im}\,\Sigma(\omega)}{[\hbar\omega - \varepsilon(\mathbf{k}) - \text{Re}\,\Sigma(\omega)]^2 + [\text{Im}\,\Sigma(\omega)]^2}. \quad (1)$$

$\mathcal{A}(\mathbf{k}, \omega)$ is again proportional to the imaginary part of the one-particle Green's function for the photoexcitation process.

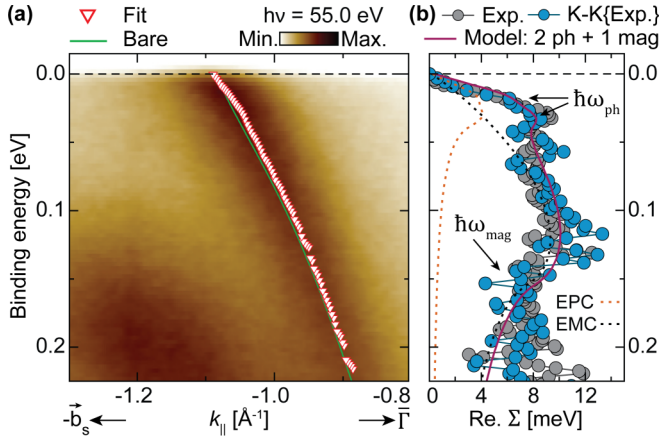

FIG. 2. EBC in the spin minority band along $-\mathbf{b}_s$ near the high-symmetry points $\bar{\mathrm{M}}$ and $\bar{\mathrm{K}}'$. (a) The measured energy band structure, overlaid with the unrenormalized (green) band and the experimentally determined, renormalized spin band position (red triangles). (b) The real self-energy Re Σ of the fitted band in (a). The Re Σ (gray) found from Eq. (2) is shown to satisfy causality with Im Σ through the Kramers-Kronig transformation (blue). A three-boson model (purple line) consisting of two distinct EPCs with energies $\hbar\omega_{\mathrm{ph}} = 18$ meV and $\hbar\omega_{\mathrm{ph}} = 36$ meV, respectively, and one EMC with energy $\hbar\omega_{\mathrm{mag}} = 154$ meV, best describes the measured line shape. The individual EPC (dashed orange) and EMC (dashed black) models are highlighted.

Notably, Eq. (1) states that for cuts through the data at constant binding energy $\hbar\omega$, $\mathcal{A}(\mathbf{k}, \omega)$ will assume a Lorentzian line profile with a peak maximum at the value of $\mathbf{k}$ where $\hbar\omega = \varepsilon(\mathbf{k}) + \mathrm{Re}\,\Sigma(\omega)$ and a full width at half maximum $\mathrm{FWHM} = 2|\mathrm{Im}\,\Sigma(\omega)|$. By extracting and fitting momentum distribution curves (MDCs) at each measured energy one can then estimate the real and imaginary components of Σ as [25,27,36]:

$$\mathrm{Re}\,\Sigma(\omega) = E(\mathbf{k}) - \varepsilon(\mathbf{k}), \tag{2}$$

$$|\mathrm{Im}\,\Sigma(\omega)| = |d\varepsilon/d\mathbf{k}| \times |\Delta\mathbf{k}|. \tag{3}$$

Here $E(\mathbf{k}) \equiv \hbar\omega_{\mathbf{k}}$ is the measured energy band dispersion, $\varepsilon(\mathbf{k})$ is the unrenormalized band, $|d\varepsilon/d\mathbf{k}|$ is the absolute value of its gradient, and $|\Delta\mathbf{k}|$ is the measured peak half-width along the in-plane momentum ($k_{||}$) axis.

In Fig. 2(a) the fitted position of an interacting spin minority band of Ni(111) is shown. This same band was also displayed along $-\mathbf{b}_s$ in Fig. 1(c) but measured at a different $\mathbf{k}_z$ position in the bulk BZ. Several clear deviations between the fitted band position and the one-particle band structure can be seen within 225 meV of E_F, and sudden energy broadenings along the measured band position are also apparent. Both features are typical hallmarks of electron-boson coupling (EBC) [23–27]. The experimental self-energy of the band was therefore estimated by a self-consistent analysis procedure based on Eqs. (2) and (3) (see Sec. IV B for details). Its Re Σ is shown in Fig. 2(b) and is demonstrated to satisfy causality with Im Σ via a Kramers-Kronig (K-K) transformation [37,38]. From the spectrum a steep rise up to ≈35 meV can be observed, followed by a broad feature over a larger energy range. The former can be related to the apparent "kink" in the measured band position in Fig. 2(a) and is a characteristic signature of EPC [36–40]. Its energy is furthermore in approximate agreement with the Debye temperature of bulk Ni ($\Theta_D \approx 477$ K) [41].

Deconvolving Re Σ by an integral inversion method produces the energy-dependent Eliashberg function $\alpha^2F(\omega)$, distinguishing the boson modes that renormalize the locally measured electron band by their interaction energy [42–47]. The resultant $\alpha^2F(\omega)$, as detailed in the Supplemental Material [32], immediately suggests two distinct EBCs with energies matching the surface and bulk-derived vibrations of Ni [48–51]. In addition, it contains several prominent couplings above the Ni Debye energy $k_B\Theta_D$ and up to $E_B \approx 140$ meV [32].

Given the ferromagnetic nature of the system, interactions between electrons and magnons can occur [24–27]. At a glance, signatures of EMC from ARPES should crudely resemble those of EPC. However, the two will typically have separate coupling energies, and their functional shape should also differ because of their intrinsically different energy dispersion relations [29,32]. Alternatively, phonon or magnon mode-specific renormalizations can — under certain simplifying assumptions — be predicted from first-principles calculations [52–55]. However, discovering all the possible couplings requires an overview of the occupied bosonic modes, a detailed knowledge of the EBC matrix elements, and all the possible propagation channels between initial and final states that preserve energy and momentum. This is a complicated task already in lighter elements [47,53,55], and an accurate determination is beyond the scope of this work. From our data we therefore attempt only a preliminary assignment of coupling modes, basing our suggestions on the distinct energies of the phonons and magnons in Ni.

Resultingly, the interactions at $E_B < k_B\Theta_D$ are assigned to EPC with surface- and bulk-derived phonons [48,50,51]. Next, inelastic scattering measurements of bulk Ni have verified three different and characteristic magnon energy dispersions, namely one acoustic branch along the [111] propagation direction with $\hbar\omega_{\mathrm{ac}}^{[111]} \leqslant 175$ meV, another acoustic branch along [100] with $\hbar\omega_{\mathrm{ac}}^{[100]} \leqslant 165$ meV, and one optical [100] branch approximately between $130 \leqslant \hbar\omega_{\mathrm{op}}^{[100]} \leqslant 250$ meV [56–59]. The higher-energy signatures of $\alpha^2F(\omega)$ are thus interpreted as EMC primarily with the acoustic magnons. However, some features may stem from the optical branch near its lower-energy extremum.

To disentangle the interaction strengths of the EPC and EMC, a minimalistic three-boson approximation consisting of two distinct phonon modes and one magnon mode was fitted to the data from Fig. 2(b). This model reproduced the main features of Re Σ, with energies $\hbar\omega_{\mathrm{ph}}^{(1)} = 18 \pm 5$ meV, $\hbar\omega_{\mathrm{ph}}^{(2)} = 36 \pm 5$ meV, and $\hbar\omega_{\mathrm{mag}} = 154 \pm 6$ meV. The associated dimensionless EPC strength $\lambda_{\mathrm{ph}} = 0.20 \pm 0.05$ is in excellent agreement with previous estimates from calculations and surface-sensitive inelastic scattering measurements [60,61]. Furthermore, the EMC strength $\lambda_{\mathrm{mag}} = 0.17 \pm 0.01$ approximately matches the value previously reported from ARPES [27]. The total EBC strength $\lambda_{\mathrm{tot}} = \lambda_{\mathrm{ph}} + \lambda_{\mathrm{mag}}$ from the model is also consistent within the value found

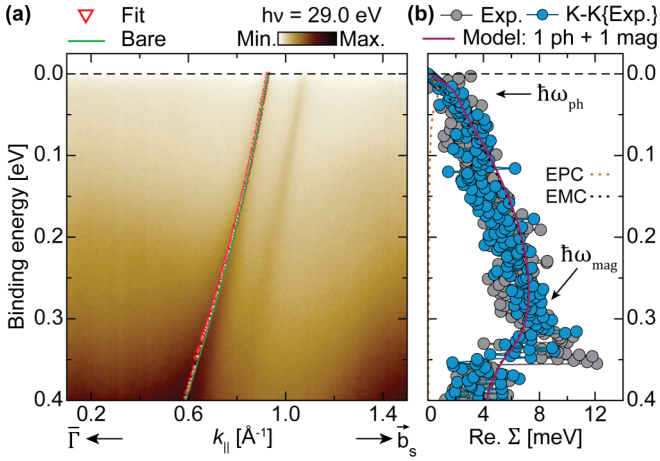

FIG. 3. EBC in the spin-minority band along $+\mathbf{b}_s$ near the high-symmetry points $\bar{M}'$ and $\bar{K}$. (a) The measured energy dispersion of the spin bands overlaid with the unrenormalized band (green) and the experimentally determined, renormalized spin minority band position (red triangles). (b) The real self-energy Re Σ (gray) of the fitted band in (a), shown to be consistent with the imaginary part Im Σ through the K-K transformation (blue). A two-boson model (purple line) consisting of one EPC at $\hbar\omega_{ph} = 23$ meV, and one EMC at $\hbar\omega_{mag} = 340$ meV, best describes the measured line shape. The individual EPC (dashed orange) and EMC (dashed black) models have been highlighted.

from integral inversion analysis within the uncertainty (see Sec. IV B).

Interestingly, the innermost spin minority contour near the $\bar{K}$ and $\bar{M}'$ points revealed additional EBC modes with different characteristic energies and strengths [32]. This spin minority band, as measured and fitted along direction $+\mathbf{b}_s$, is shown in Fig. 3 together with the real part of its K-K consistent self-energy. Coupling can be readily distinguished up to $E_B \approx 350$ meV, i.e., well beyond the maximum phonon and magnon energy values measured by inelastic scattering [48,57]. However, calculations have indicated that the already-mentioned optical magnon branch should exist in this energy range and out to the BZ boundary in $\mathbf{k}$ [62]. EMC at similar energies in a different Ni spin minority band has also been reported [27]. We thus assign the higher-energy signatures to coupling primarily with optical magnons.

Similarly, the interactions as seen from Fig. 3(b) were quantified using a best-fit model consisting of two dominant boson modes: one EPC at $\hbar\omega_{ph} = 23 \pm 12$ meV with $\lambda_{ph} = 0.05 \pm 0.03$ and one EMC at $\hbar\omega_{mag} = 340 \pm 13$ meV with $\lambda_{mag} = 0.06 \pm 0.01$. The former is situated amidst the phonon energy range and suggests a weak coupling to either of the known vibrational modes [48,50,51]. The latter indicates weak coupling to the optical magnons as already discussed [62]. Extracting $\alpha^2F(\omega)$ by integral inversion yields interactions at similar energies and with a matching total EBC strength λ_{tot} [32]. The reason behind the different participating magnon modes and the smaller λ_{tot} when compared to the EBC measured along $-\mathbf{b}_s$ [Fig. 2] is not immediately clear. Possibly, it may originate from having a different pairing of suitable initial and final electron states available at this position in the bulk BZ [63]. This hypothesis is supported by additional measurements of the same spin minority surface resonance at a different $\mathbf{k}_z$, confirming the strong momentum dependence of the EMC [32].

The estimated EBC energies and strengths λ from the two different E vs $k_{||}$ cuts along $\pm\mathbf{b}_s$ have been summarized in Table I. The coupling parameters for the same cuts measured at different $\mathbf{k}_z$ positions, i.e., using different photoexcitation energies $h\nu$, have also been presented. Their corresponding plots are shown and discussed in the Supplemental Material [32].

Finally, attention is directed towards electron-boson interactions in the spin majority states. Close to midway between $\bar{M}$ and $\bar{K}'$ a near parabolic spin majority band is found at 185 meV below E_F. This band also appeared along $-\mathbf{b}_s$ in Fig. 2(a) and was found to reach a global band maximum when measured with $h\nu = 21.2$ eV [32]. In Fig. 4(a), the fitted spin majority band position is overlaid on the measured band structure, together with the one-particle band suggested by K-K analysis. To obtain a more accurate estimate of the band maximum, the renormalized band was asserted from a combination of MDC and energy distribution curve fits [21,39].

The resultant self-energy Σ [Fig. 4(b)] indicates an EBC at $E_B = 235$ meV, i.e., approximately 50 meV below the band maximum energy E_{BM}. This is similar to one of the EMC energies reported from the spin minority bands (see Table I). However, EMC at this energy does not satisfy the line shape of the measured Σ. Specifically, it fails to reproduce the abrupt "step" that is observed from Im Σ. In comparison, a much better fit can be achieved using an EPC model that allows coupling from E_{BM}, with $\hbar\omega_{ph} = 50 \pm 5$ meV and $\lambda_{ph} = 0.55 \pm 0.05$. The abrupt increase in the electron density of states (DOS) at the band maximum then causes a relatively large λ_{ph}

TABLE I. Measured EBC in the spin minority and majority band(s) as a function of photoexcitation energy $h\nu$. Entries marked with a "∗" are shown and discussed in the Supplemental Material [32]. The mass-enhancement factors λ_{tot} and the constituents λ_{ph} and λ_{mag} were estimated separately using different methods (see Sec. IV B). The uncertainties in λ_{tot} were obtained by propagating the uncertainty of $\alpha^2F(\omega)$ as extracted from the data [42]. All other uncertainties were estimated from a relative 5% increase in the root mean square difference between the corresponding best-fit EBC model and the data.

Figure	Fitted band dispersion	$h\nu$ (eV)	λ_{tot}	$\hbar\omega_{ph}$ (meV)	λ_{ph}	$\hbar\omega_{mag}$ (meV)	λ_{mag}	Temp. (K)
Fig. 2	Min. spin $\bar{\Gamma} \rightarrow -\mathbf{b}_s$	55.0	0.24 ± 0.06	$18, 36 \pm 5$	0.20 ± 0.05	154 ± 6	0.17 ± 0.01	21
Fig. S6*	Min. spin $\bar{\Gamma} \rightarrow -\mathbf{b}_s$	29.0	0.14 ± 0.06	32 ± 2	0.13 ± 0.02	–	–	77
Fig. 3	Min. spin $\bar{\Gamma} \rightarrow +\mathbf{b}_s$	29.0	0.08 ± 0.05	23 ± 12	0.05 ± 0.03	340 ± 13	0.06 ± 0.01	77
Fig. S7*	Min. spin $\bar{\Gamma} \rightarrow +\mathbf{b}_s$	21.2	0.20 ± 0.07	$18, 30 \pm 8$	0.12 ± 0.04	250 ± 6	0.11 ± 0.01	115
Fig. 4	Maj. spin $\bar{\Gamma} \rightarrow -\mathbf{b}_s$	21.2	0.60 ± 0.32	50 ± 5	0.55 ± 0.05	–	–	115

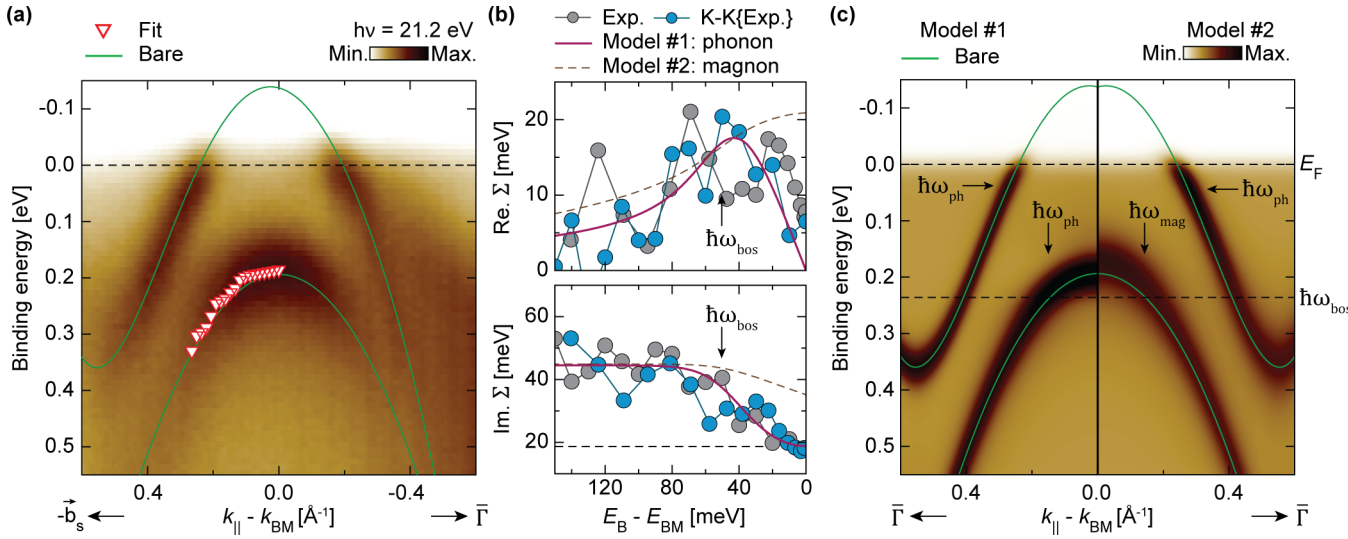

FIG. 4. EBC in the spin majority energy band along $-\mathbf{b}_s$ near the high-symmetry points $\bar{\mathrm{M}}$ and $\bar{\mathrm{K}}'$. (a) The measured electron energy dispersion along $-\mathbf{b}_s$, overlaid with the experimentally determined, renormalized position of the spin majority band (red triangles), and suggested one-particle "bare" bands for both spin configurations (in green). (b) The real and imaginary self-energies of the fitted spin majority band in (a). Each component is shown to be consistent through the K-K transformation. The EBC appears at 50 meV below the spin majority energy band maximum E_{BM}. The interaction is best described by EPC from E_{BM} with $\lambda_{ph} = 0.55$ (purple) instead of EMC from E_F (dashed gray). The added energy broadening from electron-impurity scattering and the finite instrumental resolution (dashed horizontal black line) is also shown. (c) ARPES simulations of the spin bands in (a), implementing either EMC at $\hbar\omega_{mag} = 235$ meV below E_F (right) or EPC at $\hbar\omega_{ph} = 50$ meV below E_{BM} (left) in the spin majority band. Both models have an additional EPC contribution in the spin minority band at $\hbar\omega_{ph} = 35$ meV below E_F, as suggested from the self-energy analysis summarized in Table I.

compared to the EPC found near E_F. Similarly, strong EPC in near-parabolic bands below E_F has been reported previously from ARPES but only in two-dimensional and nonmagnetic materials [64–66].

The data shown in Figs. 4(a) and 4(b) alone cannot give one definite answer about the bosonic origin of the interaction observed from the spin majority band. However, EPC appears to be more likely, based on the line shape of the Σ contributions. To further explore the origin of the observed EBC, the spectral function $\mathcal{A}(\mathbf{k}, \omega)$ from Fig. 4(a) was simulated within either of the two suggested coupling schemes. The simulations were performed using the suggested one-particle bands shown (i.e., "bare" bands, in green), broadened by the experimental resolutions, and a Fermi-Dirac distribution at the measurement temperature T (numbers in Sec. IV A). Based on additional measurements of the adjacent spin minority band (see Table I), an EPC near E_F with $\hbar\omega_{ph} = 35$ meV and $\lambda_{ph} = 0.1$ was also included. The two simulations are shown side by side in Fig. 4(c). Within the topmost 100 meV below E_F the two suggestions are very similar, as both have the same, dominant Σ contribution from EPC in the spin minority band at $E_B = \hbar\omega_{ph} = 35$ meV. At larger binding energies, however, they reveal more striking differences. The suggested EMC significantly renormalizes the near-parabolic spin majority states, shifting these away from the one-particle energy band maximum and towards E_F. A strong energy broadening is also present throughout the simulated energy range. In comparison, EPC within the spin majority band yields a more local renormalization. Here the energy broadening is concentrated around the one-particle energy band maximum at E_{BM}, and a more pronounced kink is observed.

The simulated EPC is thus seen to better recreate the measured shape of the spin majority band [Fig. 4(a)] and its associated self-energy Σ [Fig. 4(b)]. The similar, but weaker, coupling observed from the spin minority bands (Table I) certainly confirms the presence of appreciable EPC in the system, which should also occur in the spin majority bands. Furthermore, one could argue that intraband scattering from electron-phonon interactions can, in many cases, occur with a higher probability than interband electron-magnon scattering.

III. CONCLUSIONS

In summary, we have demonstrated the existence and $\mathbf{k}_z$ dependence of both phonon- and magnon-derived quasiparticles in spin-minority, surface resonance energy bands on Ni(111). These have been disentangled based on their characteristic interaction energies and the functional form of their self-energy contributions. Different electron-magnon interactions have been observed and assigned to the distinctly different magnon modes available in the system. Previously unanticipated acoustic mode coupling has been demonstrated, and higher-energy optical mode coupling has been reaffirmed and reinterpreted, adding rigor to previous works [27,56–59,62]. The specific magnon mode that electrons interact with, and their associated coupling strengths λ_{mag}, have been shown to vary dramatically with the spin minority band position within the bulk BZ.

Additionally, a moderately strong ($\lambda > 0.5$) renormalization has been observed in bulk spin majority bands at larger binding energies. This feature is best described by electron-phonon coupling near the corresponding energy band

maximum and is (to the best of our knowledge) the first known reporting of such coupling from spin-polarized, sub-Fermi-level energy-band maxima in three-dimensional ferromagnets.

IV. METHODS

A. Sample preparation and band-structure measurements

A clean Ni(111) surface was prepared by subjecting a bulk crystal to repeated cycles of Ar^+ ion sputtering at 1 keV, followed by annealing to 500 °C for a short duration. The cleanliness of the surface was verified using low-energy electron diffraction (LEED) and X-ray photoelectron spectroscopy (XPS) of the relevant core levels (see the Supplemental Material [32]).

Energy band-structure measurements were performed at 115 K using a NanoESCA III aberration-corrected EF-PEEM equipped with a He I photoexcitation source ($h\nu = 21.2$ eV) using pass energy $E_P = 25$ eV and a 0.5 mm entrance slit to the energy filter [67]. At the mentioned settings, the instrument had E and k resolutions of approximately 50 meV and 0.02 $Å^{-1}$, respectively. Higher-energy-resolution band-structure measurements were performed at the synchrotron endstations APE-LE (Elettra, Trieste, Italy) and Bloch (MAX IV Laboratory, Lund, Sweden). At Elettra the Ni(111) crystal was cooled to $T = 77$ K and measured with an energy resolution $\Delta E = 12$ meV. At Bloch the crystal temperature was $T = 21$ K and the energy resolution $\Delta E \leqslant 8$ meV. All measurements at both facilities were performed using VG SCIENTA DA30 analyzers.

B. Self-energy Σ analysis

MDCs of the spin majority and minority bands were fitted over the relevant energy ranges using one or more Lorentzian line shapes, superimposed on a linear or polynomial background. The peak position and width (in $Å^{-1}$) of the bands at each measured energy were extracted, and in turn used to estimate Re Σ and Im Σ, respectively. An initial guess at the one-particle band was approximated by a fifth-degree polynomial over the same energy range as the fitted experimental data. Its shape was then adjusted to achieve causality between the self-energy Σ components [29,37,38,65].

To disentangle any bosonic contributions to the measured self-energies, the Eliashberg coupling function $\alpha^2F(\omega)$ was extracted from each $\Sigma(\omega, T)$ by an integral inversion method [42–47]. The constant energy offset δE of each Im Σ was assigned to broadening from a combination of electron-impurity scattering and the finite instrumental resolution [68]. Data points from the corresponding Re Σ at energies $E_B < \delta E$ were discarded to correct for distortions of the renormalized band position near E_F [47]. Any signs of electron-electron scattering were indiscernible within the energy ranges measured and therefore excluded [69,70]. From each extracted $\alpha^2F(\omega)$, the total electron mass-enhancement λ_{tot} due to EBC in the quasielastic approximation was estimated as [71]:

$$\lambda_{tot} = 2\int_0^{\omega_{max}} \frac{\alpha^2F(\omega')}{\omega'} d\omega', \tag{4}$$

where ω_{max} is the frequency of the observable bosonic mode with the highest energy.

To further quantify the individual EBC contributions to the measured Σ, linear contributions of EPCs and EMCs were simulated and compared to the line shapes found from the experimental data. Each measured Σ was fitted individually to minimize the root mean square difference to the simulation of postulated couplings at the experimental temperature T. The phonon occupancy was approximated by a three-dimensional Debye model with phonon DOS $\rho_{ph}(\omega) \propto \omega^2$ and Debye frequency ω_{max}^{ph} [72]. A similar model was used for the magnons, with a maximum frequency ω_{max}^{mag} and a magnon DOS $\rho_{mag}(\omega) \propto \omega^{1/2}$, based on the energy dispersion $\omega \propto \mathbf{q}^2$ expected for acoustic magnons [24,27].

Each linear contribution (i) to Im Σ from EBC was calculated as [36,68]:

$$\text{Im}\,\Sigma^{(i)}(\omega, T) = \pi\hbar \int_0^{\omega_{max}} \alpha^2F^{(i)}(\omega') \times [1 + 2n(\omega', T) + f(\omega + \omega', T) - f(\omega - \omega', T)]d\omega', \tag{5}$$

where $\alpha^2F^{(i)}(\omega)$ is the Eliashberg coupling function for the interaction i and $n(\omega, T)$ and $f(\omega, T)$ are boson and fermion distributions, respectively. For phonons in the isotropic Debye model, $\alpha^2F^{(i)}(\omega) = \lambda_{ph}(\omega/\omega_{max}^{ph})^2$ when $\omega < \omega_{max}^{ph}$ is assumed, with λ_{ph} being the dimensionless strength of the EPC [39]. For isotropic magnons, $\alpha^2F^{(i)}(\omega) = (\lambda_{mag}/4)(\omega/\omega_{max}^{mag})^{1/2}$ for energies $\omega < \omega_{max}^{mag}$, with λ_{mag} being the dimensionless EMC strength [24]. In each case, $\alpha^2F^{(i)}(\omega) = 0$ above ω_{max}. The Re $\Sigma^{(i)}$ corresponding to each Im $\Sigma^{(i)}$ was found using the K-K transform [37,38].

C. First-principles calculations

First-principles calculations were performed using the DFT software package QuantumESPRESSO. A plane wave basis with ultrasoft pseudopotentials and the local density approximation for the exchange-correlation energy were used. Bulk calculations were performed self-consistently in a system with periodic boundary conditions, and k points were sampled using a Monkhorst-Pack grid of 12 × 12 × 12. The cut-off energy was 50 Ry and the convergence threshold 1×10^{-8} Ry. The surface states were calculated using a slab geometry with 24 atomic layers and a separation of 15 Å between slabs. Sampling of k points was done using a Monkhorst-Pack grid of 10 × 10 × 1. The cut-off energy was 40 Ry and the convergence threshold 1×10^{-6} Ry.

To simulate the ARPES spectra visible when using photoexcitation energy of $h\nu = 21.2$ eV, the crystal momentum of the emitted electrons was selected according to the free-electron final-state approximation of photoemission [20,73]. In the extended BZ, a hemispherical cut with a radius $|\mathbf{k}_F|$ corresponding to the free-electron final-state wave vector at E_F was calculated around Γ. Only the states at the Fermi surface coinciding with the hemispherical shell were projected onto the (111) plane. See for instance Refs. [35,74] for additional details on the methodology. In determining the sphere radius, a work function $\phi_s = 4.9$ eV (found by measurement, see the Supplemental Material [32]) and the value $V_0 = 10.7$ eV [74] for the inner potential was assumed. The corresponding projected bulk states yielded the spin-polarized constant energy

surface displayed in Fig. 1(b), matching the positions of the measured bands within an 8% difference. We assign this error to uncertainties in the ϕ_s and V_0 values used to determine the radius $|\mathbf{k}_F|$ of the hemisphere.

ACKNOWLEDGMENTS

This work was partly supported by the Research Council of Norway (RCN), Projects No. 324183, No. 315330, and No. 262633. Additional financial support was received from CALIPSOplus, under Grant Agreement No. 730872 from the EU Framework Programme for Research and Innovation HORIZON 2020. We acknowledge Elettra Sincrotrone Trieste and MAX IV Laboratory for providing time on their beamlines APE-LE and Bloch, respectively, and for technical support. Research conducted at MAX IV, a Swedish national user facility, is supported by the Swedish Research Council under Contract No. 2018-07152, the Swedish Governmental Agency for Innovation Systems under Contract No. 2018-04969, and Formas under Contract No. 2019-02496. We also thank T. Balasubramanian, T.-Y. Chien, B. Holst, J. R. Manson, J. Shi, A. Skarpeid, A. Sudbø, and E. Thingstad for insightful discussions on electron-boson interactions.

[1] J. Bardeen, L. N. Cooper, and J. R. Schrieffer, Theory of superconductivity, Phys. Rev. **108**, 1175 (1957).

[2] G.-H. Gweon, T. Sasagawa, S. Zhou, J. Graf, H. Takagi, D.-H. Lee, and A. Lanzara, An unusual isotope effect in a high-transition-temperature superconductor, Nature (London) **430**, 187 (2004).

[3] D. S. Inosov, J. T. Park, A. Charnukha, Y. Li, A. V. Boris, B. Keimer, and V. Hinkov, Crossover from weak to strong pairing in unconventional superconductors, Phys. Rev. B **83**, 214520 (2011).

[4] K. Gotlieb, C.-Y. Lin, M. Serbyn, W. Zhang, C. L. Smallwood, C. Jozwiak, H. Eisaki, Z. Hussain, A. Vishwanath, and A. Lanzara, Revealing hidden spin-momentum locking in a high-temperature cuprate superconductor, Science **362**, 1271 (2018).

[5] M. Oh, K. P. Nuckolls, D. Wong, R. L. Lee, X. Liu, K. Watanabe, T. Taniguchi, and A. Yazdani, Evidence for unconventional superconductivity in twisted bilayer graphene, Nature (London) **600**, 240 (2021).

[6] S. S. Saxena, P. Agarwal, K. Ahilan, F. M. Grosche, R. K. W. Haselwimmer, M. J. Steiner, E. Pugh, I. R. Walker, S. R. Julian, P. Monthoux, G. G. Lonzarich, A. Huxley, I. Sheikin, D. Braithwaite, and J. Flouquet, Superconductivity on the border of itinerant-electron ferromagnetism in UGe_2, Nature (London) **406**, 587 (2000).

[7] C. Pfleiderer, M. Uhlarz, S. M. Hayden, R. Vollmer, H. v. Löhneysen, N. R. Bernhoeft, and G. G. Lonzarich, Coexistence of superconductivity and ferromagnetism in the d-band metal $ZrZn_2$, Nature (London) **412**, 58 (2001).

[8] D. Aoki, A. Huxley, E. Ressouche, D. Braithwaite, J. Flouquet, J.-P. Brison, E. Lhotel, and C. Paulsen, Coexistence of superconductivity and ferromagnetism in URhGe, Nature (London) **413**, 613 (2001).

[9] N. J. Curro, T. Caldwell, E. D. Bauer, L. A. Morales, M. J. Graf, Y. Bang, A. V. Balatsky, J. D. Thompson, and J. L. Sarrao, Unconventional superconductivity in $PuCoGa_5$, Nature (London) **434**, 622 (2005).

[10] Y. Kamihara, T. Watanabe, M. Hirano, and H. Hosono, Iron-based layered superconductor $La[O_{1-x}\ F_x]FeAs$ ($x = 0.05 - 0.12$) with $T_c = 26$ K, J. Am. Chem. Soc. **130**, 3296 (2008).

[11] N. Karchev, Magnon exchange mechanism of ferromagnetic superconductivity, Phys. Rev. B **67**, 054416 (2003).

[12] G. M. Zhang, Z. Y. Lu, and T. Xiang, Superconductivity mediated by the antiferromagnetic spin wave in chalcogenide iron-based superconductors, Phys. Rev. B **84**, 052502 (2011).

[13] M. Kargarian, D. K. Efimkin, and V. Galitski, Amperean pairing at the surface of topological insulators, Phys. Rev. Lett. **117**, 076806 (2016).

[14] X. Gong, M. Kargarian, A. Stern, D. Yue, H. Zhou, X. Jin, V. M. Galitski, V. M. Yakovenko, and J. Xia, Time-reversal symmetry-breaking superconductivity in epitaxial bismuth/nickel bilayers, Sci. Adv. **3**, e1602579 (2017).

[15] N. Rohling, E. L. Fjærbu, and A. Brataas, Superconductivity induced by interfacial coupling to magnons, Phys. Rev. B **97**, 115401 (2018).

[16] E. Thingstad, E. Erlandsen, and A. Sudbø, Eliashberg study of superconductivity induced by interfacial coupling to antiferromagnets, Phys. Rev. B **104**, 014508 (2021).

[17] K. Mæland, H. I. Røst, J. W. Wells, and A. Sudbø, Electron-magnon coupling and quasiparticle lifetimes on the surface of a topological insulator, Phys. Rev. B **104**, 125125 (2021).

[18] J. M. Ok, C. I. Kwon, O. E. Ayela Valenzuela, S. Kim, R. D. McDonald, J. Kim, E. S. Choi, W. Kang, Y. J. Jo, C. Kim, E. G. Moon, Y. K. Kim, and J. S. Kim, Strong antiferromagnetic proximity coupling in the heterostructure superconductor $Sr_2VO_{3-\delta}$ FeAs, Phys. Rev. B **105**, 214505 (2022).

[19] S. D. Kevan and W. Eberhardt, *Angle-Resolved Photoemission: Theory and Current Applications*, edited by S. D. Kevan (Elsevier, Amsterdam, 1992), Chaps. 2 and 4.

[20] A. Damascelli, Probing the electronic structure of complex systems by ARPES, Phys. Scr. **2004**, 61 (2004).

[21] Ph. Hofmann, I. Y. Sklyadneva, E. D. L. Rienks, and E. V. Chulkov, Electron–phonon coupling at surfaces and interfaces, New J. Phys. **11**, 125005 (2009).

[22] S. Hüfner, *Photoelectron Spectroscopy: Principles and Applications* (Springer Science & Business Media, Berlin, 2013), Chap. 1.

[23] S. Hüfner, *Very High Resolution Photoelectron Spectroscopy*, Vol. 715 (Springer, Berlin, 2007), Chap. 2.4.

[24] J. Schäfer, D. Schrupp, E. Rotenberg, K. Rossnagel, H. Koh, P. Blaha, and R. Claessen, Electronic quasiparticle renormalization on the spin wave energy scale, Phys. Rev. Lett. **92**, 097205 (2004).

[25] X. Cui, K. Shimada, M. Hoesch, Y. Sakisaka, H. Kato, Y. Aiura, S. Negishi, M. Higashiguchi, Y. Miura, H. Namatame, and M. Taniguchi, High-resolution angle-resolved photoemission spectroscopy of iron: A study of the self-energy, J. Magn. Magn. Mater. **310**, 1617 (2007).

[26] X. Cui, K. Shimada, M. Hoesch, Y. Sakisaka, H. Kato, Y. Aiura, M. Higashiguchi, Y. Miura, H. Namatame, and M. Taniguchi, Angle-resolved photoemission spectroscopy study of Fe(110) single crystal: Many-body interactions between quasi-particles at the Fermi level, Surf. Sci. **601**, 4010 (2007).

[27] A. Hofmann, X. Y. Cui, J. Schäfer, S. Meyer, P. Höpfner, C. Blumenstein, M. Paul, L. Patthey, E. Rotenberg, J. Bünemann, F. Gebhard, T. Ohm, W. Weber, and R. Claessen, Renormalization of bulk magnetic electron states at high binding energies, Phys. Rev. Lett. **102**, 187204 (2009).

[28] E. Młyńczak, M. C. T. D. Müller, P. Gospodarič, T. Heider, I. Aguilera, G. Bihlmayer, M. Gehlmann, M. Jugovac, G. Zamborlini, C. Tusche, S. Suga, V. Feyer, L. Plucinski, C. Friedrich, S. Blügel, and C. M. Schneider, Kink far below the fermi level reveals new electron-magnon scattering channel in Fe, Nat. Commun. **10**, 505 (2019).

[29] F. Mazzola, C.-M. Yim, V. Sunko, S. Khim, P. Kushwaha, O. J. Clark, L. Bawden, I. Marković, D. Chakraborti, T. K. Kim, M. Hoesch, A. P. Mackenzie, P. Wahl, and P. D. C. King, Tuneable electron–magnon coupling of ferromagnetic surface states in $PdCoO_2$, npj Quantum Mater. **7**, 20 (2022).

[30] B. Andres, M. Weinelt, H. Ebert, J. Braun, A. Aperis, and P. M. Oppeneer, Strong momentum-dependent electron–magnon renormalization of a surface resonance on iron, Appl. Phys. Lett. **120**, 202404 (2022).

[31] T. L. Yu, M. Xu, W. T. Yang, Y. H. Song, C. H. P. Wen, Q. Yao, X. Lou, T. Zhang, W. Li, X. Y. Wei, J. K. Bao, G. H. Cao, P. Dudin, J. D. Denlinger, V. N. Strocov, H. C. Xu, and D. L. Feng, Strong band renormalization and emergent ferromagnetism induced by electron-antiferromagnetic-magnon coupling, Nat. Commun. **13**, 6560 (2022).

[32] See Supplemental Material at http://link.aps.org/supplemental/10.1103/PhysRevB.109.035137 for details on the sample preparation, LEED, XPS and work function measurements, additional ARPES data, and further details on the self-energy analysis.

[33] C. Tserkezis, N. Stefanou, G. Gantzounis, and N. Papanikolaou, Photonic surface states in plasmonic crystals of metallic nanoshells, Phys. Rev. B **84**, 115455 (2011).

[34] D. Liebowitz and N. J. Shevchik, Free-electron final-state model and angle-resolved photoemission from a Ag(111) surface, Phys. Rev. B **17**, 3825 (1978).

[35] P. Aebi, J. Osterwalder, R. Fasel, D. Naumović, and L. Schlapbach, Fermi surface mapping with photoelectrons at UV energies, Surf. Sci. **307-309**, 917 (1994).

[36] J. E. Gayone, C. Kirkegaard, J. W. Wells, S. V. Hoffmann, Z. Li, and Ph. Hofmann, Determining the electron-phonon mass enhancement parameter λ on metal surfaces, Appl. Phys. A **80**, 943 (2005).

[37] A. A. Kordyuk, S. V. Borisenko, A. Koitzsch, J. Fink, M. Knupfer, and H. Berger, Bare electron dispersion from experiment: Self-consistent self-energy analysis of photoemission data, Phys. Rev. B **71**, 214513 (2005).

[38] I. Pletikosić, M. Kralj, M. Milun, and P. Pervan, Finding the bare band: Electron coupling to two phonon modes in potassium-doped graphene on Ir(111), Phys. Rev. B **85**, 155447 (2012).

[39] S. LaShell, E. Jensen, and T. Balasubramanian, Nonquasiparticle structure in the photoemission spectra from the Be(0001) surface and determination of the electron self energy, Phys. Rev. B **61**, 2371 (2000).

[40] M. Higashiguchi, K. Shimada, K. Nishiura, X. Cui, H. Namatame, and M. Taniguchi, Energy band and spin-dependent many-body interactions in ferromagnetic Ni(110): A high-resolution angle-resolved photoemission study, Phys. Rev. B **72**, 214438 (2005).

[41] G. Stewart, Measurement of low-temperature specific heat, Rev. Sci. Instrum. **54**, 1 (1983).

[42] M. Jarrell and J. E. Gubernatis, Bayesian inference and the analytic continuation of imaginary-time quantum Monte Carlo data, Phys. Rep. **269**, 133 (1996).

[43] J. E. Gubernatis, M. Jarrell, R. N. Silver, and D. S. Sivia, Quantum Monte Carlo simulations and maximum entropy: Dynamics from imaginary-time data, Phys. Rev. B **44**, 6011 (1991).

[44] J. Shi, S.-J. Tang, B. Wu, P. T. Sprunger, W. L. Yang, V. Brouet, X. J. Zhou, Z. Hussain, Z.-X. Shen, Z. Zhang, and E. W. Plummer, Direct extraction of the Eliashberg function for electron-phonon coupling: A case study of Be($10\bar{1}0$), Phys. Rev. Lett. **92**, 186401 (2004).

[45] S.-J. Tang, J. Shi, B. Wu, P. T. Sprunger, W. L. Yang, V. Brouet, X. J. Zhou, Z. Hussain, Z.-X. Shen, Z. Zhang, and E. W. Plummer, A spectroscopic view of electron–phonon coupling at metal surfaces, Phys. Status Solidi B **241**, 2345 (2004).

[46] T. Y. Chien, E. D. L. Rienks, M. F. Jensen, Ph. Hofmann, and E. W. Plummer, Anisotropic electron-phonon coupling on a two-dimensional circular Fermi contour, Phys. Rev. B **80**, 241416(R) (2009).

[47] T. Y. Chien, X. He, S.-K. Mo, M. Hashimoto, Z. Hussain, Z.-X. Shen, and E. W. Plummer, Electron-phonon coupling in a system with broken symmetry: Surface of Be(0001), Phys. Rev. B **92**, 075133 (2015).

[48] R. J. Birgeneau, J. Cordes, G. Dolling, and A. D. B. Woods, Normal modes of vibration in nickel, Phys. Rev. **136**, A1359 (1964).

[49] J. Szeftel, Surface phonon dispersion, using electron energy loss spectroscopy, Surf. Sci. **152-153**, 797 (1985).

[50] C. Stuhlmann and H. Ibach, Surface phonon dispersion in ultrathin nickel films on Cu(100), Surf. Sci. **219**, 117 (1989).

[51] W. Menezes, P. Knipp, G. Tisdale, and S. J. Sibener, Surface phonon spectroscopy of Ni(111) studied by inelastic electron scattering, Phys. Rev. B **41**, 5648 (1990).

[52] F. Giustino, M. L. Cohen, and S. G. Louie, Electron-phonon interaction using Wannier functions, Phys. Rev. B **76**, 165108 (2007).

[53] B. Hellsing, T. Frederiksen, F. Mazzola, T. Balasubramanian, and J. W. Wells, Phonon-induced linewidths of graphene electronic states, Phys. Rev. B **98**, 205428 (2018).

[54] C. E. Mahr, M. Czerner, and C. Heiliger, Implementation of a method for calculating temperature-dependent resistivities in the KKR formalism, Phys. Rev. B **96**, 165121 (2017).

[55] Z. He, A.-A. Sun, and S.-P. Gao, Electron-phonon scattering and stacking sequences in hexagonal boron nitride: An *ab initio* study, Phys. Rev. B **108**, 165108 (2023).

[56] H. A. Mook and D. Tocchetti, Neutron-scattering measurements of the generalized susceptibility $\chi(q, e)$ for Ni, Phys. Rev. Lett. **43**, 2029 (1979).

[57] H. A. Mook and D. M. Paul, Neutron-scattering measurement of the spin-wave spectra for nickel, Phys. Rev. Lett. **54**, 227 (1985).

[58] H. A. Mook, D. M. Paul, and S. Hayden, Temperature dependence of the high-energy magnetic excitations for Ni, Phys. Rev. B **38**, 12058 (1988).

[59] N. B. Brookes, D. Betto, K. Cao, Y. Lu, K. Kummer, and F. Giustino, Spin waves in metallic iron and nickel measured by soft x-ray resonant inelastic scattering, Phys. Rev. B **102**, 064412 (2020).

[60] D. A. Papaconstantopoulos, L. L. Boyer, B. M. Klein, A. R. Williams, V. L. Morruzzi, and J. F. Janak, Calculations of the superconducting properties of 32 metals with $z \leqslant 49$, Phys. Rev. B **15**, 4221 (1977).

[61] B. Holst, G. Alexandrowicz, N. Avidor, G. Benedek, G. Bracco, W. E. Ernst, D. Farías, A. P. Jardine, K. Lefmann, J. R. Manson, R. Marquardt, S. Miret Artés, S. J. Sibener, J. W. Wells, A. Tamtögl, and W. Allison, Material properties particularly suited to be measured with helium scattering: Selected examples from 2D materials, van der Waals heterostructures, glassy materials, catalytic substrates, topological insulators and superconducting radio frequency materials, Phys. Chem. Chem. Phys. **23**, 7653 (2021).

[62] J. F. Cooke, J. A. Blackman, and T. Morgan, New interpretation of spin-wave behavior in nickel, Phys. Rev. Lett. **54**, 718 (1985).

[63] Ph. Hofmann, The surfaces of bismuth: Structural and electronic properties, Prog. Surf. Sci. **81**, 191 (2006).

[64] F. Mazzola, J. W. Wells, R. Yakimova, S. Ulstrup, J. A. Miwa, R. Balog, M. Bianchi, M. Leandersson, J. Adell, Ph. Hofmann, and T. Balasubramanian, Kinks in the σ band of graphene induced by electron-phonon coupling, Phys. Rev. Lett. **111**, 216806 (2013).

[65] F. Mazzola, T. Frederiksen, T. Balasubramanian, Ph. Hofmann, B. Hellsing, and J. W. Wells, Strong electron-phonon coupling in the σ band of graphene, Phys. Rev. B **95**, 075430 (2017).

[66] H. I. Røst, S. P. Cooil, A. C. Åsland, J. Hu, A. Ali, T. Taniguchi, K. Watanabe, B. D. Belle, B. Holst, J. T. Sadowski, F. Mazzola, and J. W. Wells, Phonon-mediated quasiparticle lifetime renormalizations in few-layer hexagonal boron nitride, Nano Lett. **23**, 7539 (2023).

[67] M. Escher, N. Weber, M. Merkel, B. Krömker, D. Funnemann, S. Schmidt, F. Reinert, F. Forster, S. Hüfner, P. Bernhard, C. Ziethen, H. Elmers, and G. Schönhense, NanoESCA: imaging UPS and XPS with high energy resolution, J. Electron Spectrosc. Relat. Phenom. **144-147**, 1179 (2005).

[68] T. Valla, A. V. Fedorov, P. D. Johnson, and S. L. Hulbert, Many-body effects in angle-resolved photoemission: Quasiparticle energy and lifetime of a Mo(110) surface state, Phys. Rev. Lett. **83**, 2085 (1999).

[69] P. Echenique, R. Berndt, E. Chulkov, T. Fauster, A. Goldmann, and U. Höfer, Decay of electronic excitations at metal surfaces, Surf. Sci. Rep. **52**, 219 (2004).

[70] E. V. Chulkov, J. Kliewer, R. Berndt, V. M. Silkin, B. Hellsing, S. Crampin, and P. M. Echenique, Hole dynamics in a quantum-well state at Na/Cu(111), Phys. Rev. B **68**, 195422 (2003).

[71] G. Grimvall, *The Electron-Phonon Interaction in Metals* (North-Holland, Amsterdam, 1981).

[72] B. Hellsing, A. Eiguren, and E. V. Chulkov, Electron-phonon coupling at metal surfaces, J. Phys.: Condens. Matter **14**, 5959 (2002).

[73] J. Osterwalder, Spin-polarized photoemission, in *Magnetism: A Synchrotron Radiation Approach*, edited by E. Beaurepaire, H. Bulou, F. Scheurer, and J.-P. Kappler (Springer, Berlin, 2006), pp. 95–120.

[74] P. Aebi, T. J. Kreutz, J. Osterwalder, R. Fasel, P. Schwaller, and L. Schlapbach, k-space mapping of majority and minority bands on the Fermi surface of nickel below and above the Curie temperature, Phys. Rev. Lett. **76**, 1150 (1996).